
Mapping Nanoscale Electrostatic Field Fluctuations Around Graphene Dislocation Cores Using 4D-STEM

*Matthew J. Coupin¹, Yi Wen², Sungwoo Lee^{3,4}, Anshul Saxena^{5,6}, Colin Ophus⁷, Christopher S. Allen^{2,8},
Angus I. Kirkland^{2,8,9}, Narayana R. Aluru^{1,5,6}, Gun-Do Lee^{3,4}, Jamie H. Warner^{1,5*}*

¹Materials Science and Engineering Program, Texas Materials Institute, The University of Texas at
Austin, Texas 78712, USA

²Department of Materials, University of Oxford, Parks Road, Oxford OX1 3PH, United Kingdom

³Department of Materials Science & Engineering, Seoul National University, Seoul 08826, Republic
of Korea

⁴Research Institute of Advanced Materials, Seoul National University, Seoul 08826, Republic of
Korea

⁵Walker Department of Mechanical Engineering, The University of Texas at Austin, Austin, Texas,
78712, USA

⁶Oden Institute for Computational Engineering and Sciences, The University of Texas at Austin,
Austin, Texas 78712, USA

⁷National Center for Electron Microscopy, Molecular Foundry, Lawrence Berkeley National
Laboratory, One Cyclotron Road, Building 67, Berkeley, CA, 94720

⁸Electron Physical Science Imaging Centre, Diamond Light Source Ltd., Didcot OX11 0DE, UK

⁹Rosalind Franklin Institute, Harwell Science and Innovation Campus, Didcot OX11 0QX, UK

Email: Jamie.warner@austin.utexas.edu

1 *Abstract*

2 Defects in crystalline lattices cause modulation of the atomic density and this leads to variations in
3 the associated electrostatics at the nanoscale. Mapping these spatially varying charge fluctuations
4 using transmission electron microscopy has typically been challenging due to complicated contrast
5 transfer inherent to conventional phase contrast imaging. To overcome this, we used four-
6 dimensional scanning transmission electron microscopy (4D-STEM) to measure electrostatic fields
7 near point dislocations in a monolayer. The asymmetry of the atomic density in a (1,0) edge
8 dislocation core in graphene yields a local enhancement of electric field in part of the dislocation
9 core. Through experiment and simulation, the increased electric field magnitude is shown to arise
10 from ‘long-range’ interactions from beyond the nearest atomic neighbor. These results provide
11 insights into the use of 4D-STEM to quantify electrostatics in thin materials and map out the lateral
12 potential variations that are important for molecular and atomic bonding through Coulombic
13 interactions.

14 **KEYWORDS:** 4D-STEM, 2D materials, line dislocation, TEM, graphene

15

16 Defects are of principal importance to materials science due to their profound influence on the
17 mechanical, electronic, and magnetic properties of materials. 2D materials are host to all defects that
18 can exist within a two-dimensional plane, including point vacancies, substitutions, and topological
19 dislocations [1]. In graphene, edge dislocations exist as a pair of pentagon-heptagon dislocation cores
20 joined by a missing row of zig-zag atoms, depicted schematically in supporting figure 1. Similar
21 pentagon-heptagon cores can be found along low-angle grain boundaries and have been theoretically
22 predicted to significantly alter graphene yield strength as a function of heptagon-pentagon core
23 density and spatial distribution [2, 3]. Topological edge dislocations and grain boundaries have both
24 been shown to locally alter the electronic density of states, with Van Hove singularities near within
25 ± 0.5 eV of the Dirac point predicted theoretically [4] in graphene and observed experimentally [5]

1 via STM in graphene and highly ordered pyrolytic graphite (HOPG) [6]. Ferromagnetic moments
2 have been theoretically predicted to emerge from pentagonal rings in otherwise diamagnetic
3 graphene [7], and low-angle grain boundaries, which can yield similarly structured defects, have
4 been experimentally measured as ferromagnetic in HOPG using magnetic force microscopy [8].
5 Pentagon-heptagon-terminated dislocation lines in graphene are energetically stable up to high
6 temperatures [9] and have been directly observed using image-corrected TEMs [10-15], primarily
7 using phase-contrast high resolution TEM. The application of scanning transmission electron
8 microscopy (STEM) for probing atomic structure and charge distributions of graphene dislocations
9 has yet to be fully explored. Recent advances in TEM detector technology have extended the
10 capabilities of STEM to the direct measurement of the local electrostatic fields with sub-Ångström
11 resolution. Because of the non-negative contrast transfer associated with differential phase contrast
12 (DPC) imaging [16, 17] 4D-STEM allows for the interpretable mapping of electrostatic fields across
13 many spatial frequencies without contrast inversion and without the need for exit wave
14 reconstruction.

15 4D-STEM refers to a wide variety of techniques—from diffraction to computational imaging—
16 that have gained popularity with the recent widespread adoption of pixelated direct electron
17 detectors. In the context of high-resolution imaging, such pixelated direct detectors have been used to
18 simultaneously image light and heavy elements by combining coherent phase imaging with
19 incoherent darkfield imaging [18, 19]. Further, pixelated detectors make possible a variety of phase
20 retrieval techniques, collectively known as ptychography, which allow for the removal of residual
21 optical aberrations for super-resolution imaging [20-22]. 4D-STEM enables the measurement of
22 projected, probe-convolved electric fields (E_z) and charge densities (ρ) as a function of two-dimensional
23 probe position on the Ångström length scale [23-25]. The PC (projected, convolved) subscripts
24 serve to remind readers that these are two-dimensional projections of three-dimensional quantities
25 and that these quantities have been convolved with the electron probe. These quantities are

1 calculated from the deflection to the center-of-mass of the STEM brightfield disk at each probe
2 position. Estimates of the center-of-mass can be extracted from pixelated detector frames or, with
3 some loss of accuracy, from a multi-channel segmented detector [25, 27]. A more rigorous definition
4 of these quantities, and details about their calculation, can be found in section 1 of the supporting
5 information.

6 4D-STEM has been used to quantitatively map charge densities in thin sections of ferroelectric
7 perovskites [28]; however, its application towards the study of defects, has been considerably more
8 limited. In the field of 2D materials 4D-STEM has revealed the presence of metallic channels in
9 MoS₂ [29] enhancement of electric fields at edges of graphene nanopores, along monolayer-bilayer
10 edges, and surrounding substitutional defects [30]. Similar electric field enhancement has been
11 observed along atomically smooth MoS₂ and WS₂ monolayer edges and was attributed to the lack of
12 atomic charge screening caused by missing atoms along the edge region [31]. However, Wen et al
13 showed that the quantitative evaluation of the electric field strengths at edges is difficult due to
14 probe-size dependent attenuation of spatial frequencies. Nevertheless, if one assumes that probe
15 aberrations and incoherencies are constant during a single 4D-STEM scan it becomes possible to
16 qualitatively map the spatial profile of electrostatic fields. 4D-STEM has been used to study point
17 defects in 2D materials including graphene [30], hBN [32], and TMDs [33], with a high degree of
18 sensitivity to atom number and location. However, to date, studies on dislocations have yet to be
19 reported. (1, 0) dislocation cores differ from most other vacancies and point defects in that all atoms
20 remain fully coordinated and lack dangling bonds. (1,0) dislocation cores also lack rotational
21 symmetry, which allows for the electrostatic influence of atoms at distances greater than a single
22 bond length to contribute to the measured electrostatic field fluctuations. Monovacancies tend to
23 relax into a non-rotationally symmetric configuration (r-MV); however, thermal or electron-beam-
24 induced motion can easily cause r-MVs to rotate into any of three stable configurations, complicating
25 their study in the TEM [34]. Nanoscale mapping of electric field fluctuations will help the

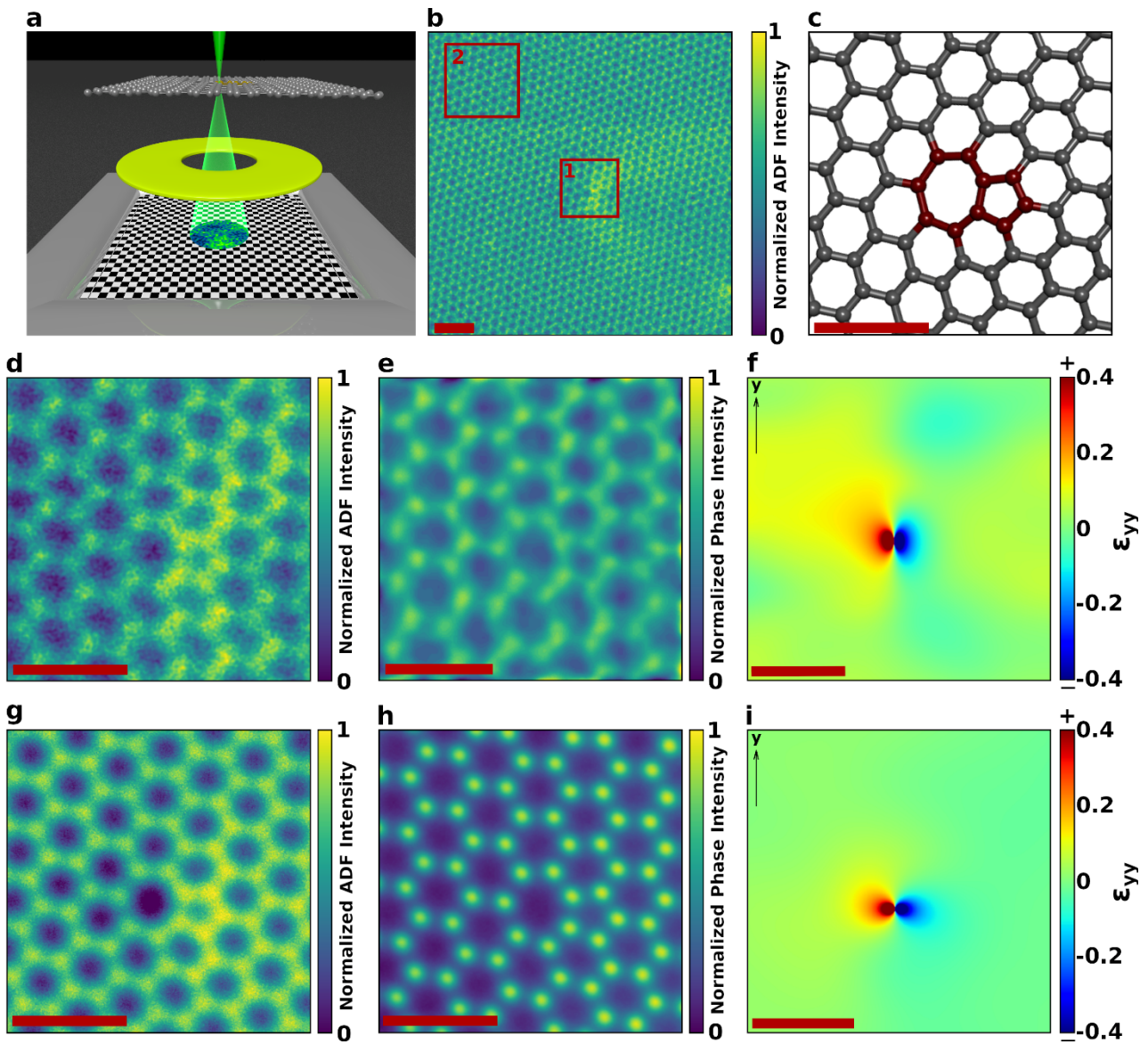
understanding of the surface potential experienced by adsorbed atoms and molecules, improving the understanding of surface adsorption and diffusion. The strong interaction between molecules and defects is well known, but the direct relationship between atomic charge distribution and surface phenomena warrants further investigation.

In this paper, 4D-STEM is used to map electrostatic fields and charge densities within and around (1, 0) dislocation cores in graphene that are sufficiently far away from other dislocation cores and perturbations such as edges, that they can be considered as isolated idealized heptagon-pentagon ring pairs. This is achieved by using an *in-situ* heating holder to remove all surface contamination at 700°C, and provide ultraclean graphene for intrinsic structural studies. Experimental measurements are validated through careful 4D-STEM image simulations, with particular attention paid to the effect of lens aberrations and partial coherence, along with calculations from density functional theory.

Results

A schematic overview of 4D-STEM with simultaneous annular darkfield (ADF) acquisition is presented in figure 1a. In figure 1 4D-STEM detector frames are used to produce phase images (Fig. 1b) by integrating the two-channel signal associated with the x and y deflections to the center-of-mass of the brightfield disk (Supporting Eqn. 6, 7). ADF-STEM produces only a single gray value at each probe position and is therefore capable of vastly reduced pixel dwell times as compared to 4D-STEM. As a result, ADF-STEM remains indispensable for navigation and overview during the experiment and is especially useful for measurements that are sensitive to stage drift. ADF images of an isolated (1,0) dislocation core are presented in Figure 1b & 1d. Panel 1b features two highlighted regions marked with red lines. Region 1 defines the field-of-view for panels 1c - 1i, and region 2 defines the reference lattice region for geometric phase analysis (1f, 1i). The dislocation core produces a strain field (, fig. 1f, 1i) resembling a dipole, with most of the strain localized to within 2-3 bond lengths of the dislocation core. In an otherwise defect-free lattice (1, 0) dislocations cores

1 exist in pairs and are joined by a missing row of zig-zag atoms (supp. fig. 1); however, the overview
 2 image (1b) and GPA strain field (1d) indicate that this core is sufficiently distant from its partner to
 3 be considered non-interacting. ADF images (Fig. 1b, 1d) and smeared potentials (Fig. 2c) show
 4 increased brightness near the dislocation core, an effect that arises due to the out-of-plane tilt of the
 5 graphene sheet near the dislocation core. When viewed in projection, the lateral distances of the
 6 carbon atoms appear to be shortened, so that convolution with the electron probe yields an elevated
 7 brightness in that area.



8

9 **Figure 1: Overview of experimental data** a) Schematic overview of experiment, showing the
 10 converged electron probe, HAADF detector, and the STEM brightfield disk associated with a given

1 probe position projected onto a pixelated direct electron detector. b) Overview HAADF image of a
2 (1, 0) dislocation core. Scale bar indicates 1 nm. c) Atomic model of the (1, 0) dislocation core. d, g)
3 Experimental and simulated high-magnification HA-ADF images of the same dislocation core, field-
4 of-view is given by inset region #1 in panel (b). e, h) Experimental and simulated phase images
5 calculated with coherent 4D-STEM data. Field of view is also given by inset region #3 in panel (b).
6 Further explanation of how phase images can be calculated from 4D-STEM data can be found in the
7 section 2 of the supporting information. f, i) Experimental and simulated geometric phase analysis
8 (GPA) strain field computed within the field-of-view indicated with #1 in panel (b). Reference
9 lattice region for GPA is indicated by region #2 defined in panel (b). Simulations given in g & h
10 represent idealized microscope conditions without lens aberrations. Scale bars in panels c-i indicate
11 5Å.

12

13 Figure 2 presents the results of 4D-STEM electric field maps of the dislocation defect presented in
14 Fig. 1. Local enhancement of ϕ is most pronounced on one side of the seven-membered ring compared
15 to the pristine regions comprised of hexagonal carbon rings. This comparison is depicted in figure 2k
16 using a line plot which spans several hexagonal carbon rings before and after crossing the dislocation
17 core. Further comparison of experimentally measured electrostatic field intensity between the
18 pentagon and the surrounding carbon lattice is provided in supporting figure 2, with the effect of
19 aberrations studied using simulation in supporting figures 3 – 5. Because carbon atoms are separated
20 by the diameter of the seven-membered ring, ϕ is elevated around its entire inner perimeter. Further,
21 supporting figure 6 shows that the spatial profiles of DFT-derived ϕ , DFT-based 4D-STEM image
22 simulation, and independent atom model (IAM) based 4D-STEM simulation all agree closely for this
23 system, and that electrostatic field magnitude is indeed maximized on the side of the heptagon that
24 adjoins the pentagon. Details for how $E_{PC}(\mathbf{R})$ can be calculated from a converged DFT simulation are
25 presented in section 4 of the supporting information. Nevertheless, 4D-STEM simulations are
26 included to help model the effects of lens aberrations, partial coherence, and other imperfect
27 microscope conditions.

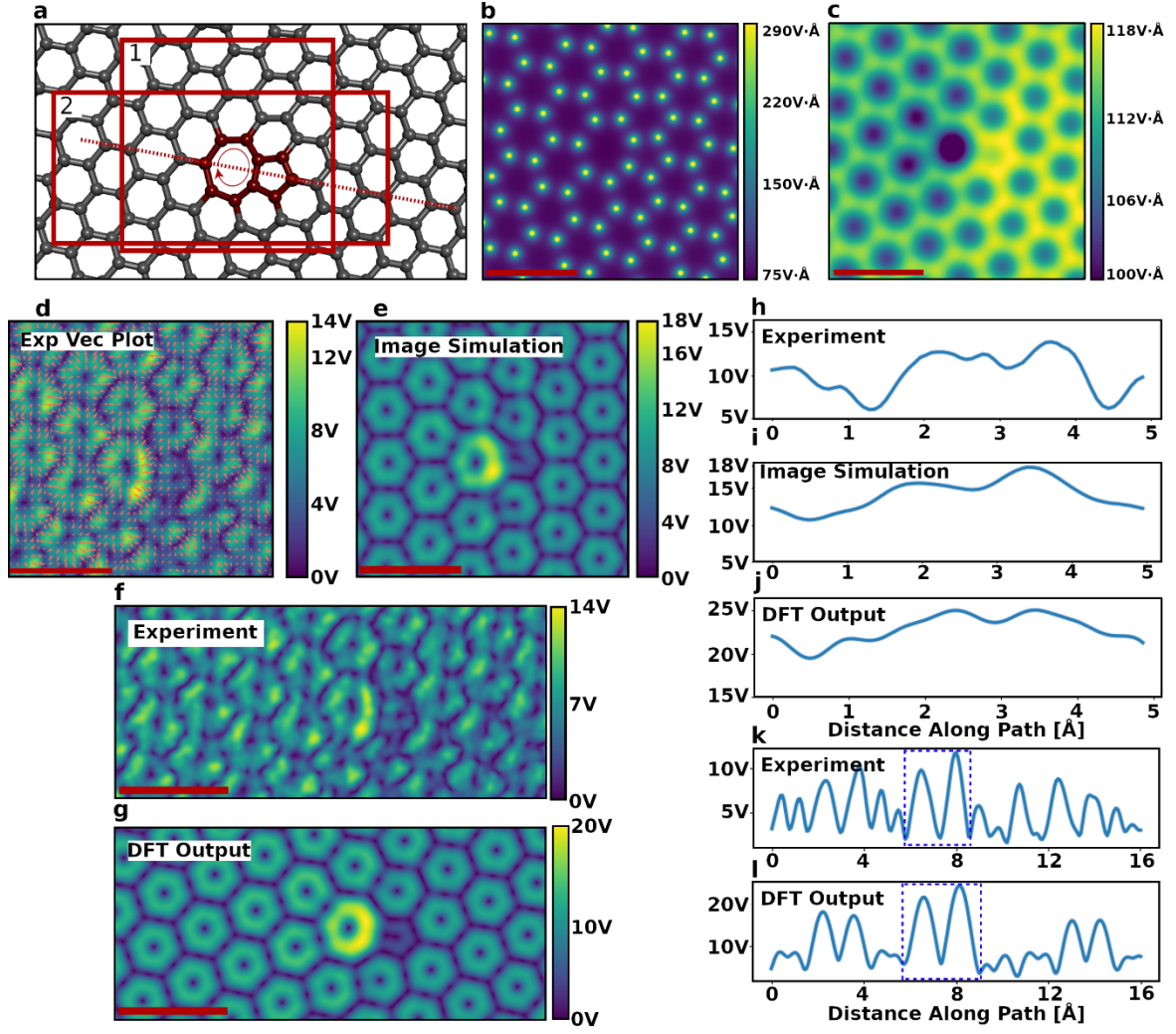


Figure 2: 4D-STEM electrostatic field results. a) Structural model of graphene sheet with (1,0) dislocation core highlighted in red. Inset region 1 defines the field of view for panels b-e. Inset region 2 defines the field of view for panels f-g. Circumferential red arrow within the heptagon of the dislocation core defines the path of the line plots shown in (h, i, j). Dotted red line indicates the path of the line profiles shown in (k, l). b) Un-smear and (c) smear ($\sigma = 0.65\text{\AA}$) electrostatic potentials from density functional theory calculations. d) Experimental E_{PC} image with arrow overlays representing the direction and magnitude of momentum transfer to the electron probe. (e) Aberrated 4D-STEM multislice simulation of $|E_{PC}|$, aberration coefficients and details on image simulation are provided in supporting table 2. Both fields-of-view correspond to inset region 1 in panel a. (f) Experimental $|E_{PC}|$ image with field of view shown in region 2 in panel a. g) $|E_{PC}|$ calculated from density functional theory calculations without image simulation, using the smear potential depicted in panel (c). (h, i, j) Circumferential line plots showing $|E_{PC}|$ results from experiment (h), 4D-STEM simulation using independent atom-derived potentials (i), and DFT calculation without image simulation (j). Lens aberrations (supporting table 2) were included in 4D-STEM simulation and are reflected in panels (e, i). Line plot paths correspond to the circular profiles denoted with an arrow in panel a). (k, l) Linear line profiles of experimental (k) and DFT-derived (l) $|E_{PC}|$ images, corresponding to panels f and g, respectively. Line profiles correspond to the dotted blue line in panel a). The interior of the heptagon ring corresponds to the region outlined with a dotted blue line. All scalebars indicate 5\AA .

Figure 3a-3c presents the charge density distributions around the dislocation core. A detailed

1 description of how projected charge density is calculated from 4D-STEM data is given in section 1
2 of the supporting information. The 2D charge density map in figure 3b has strong positive charge at
3 the atomic nucleus sites, and negative charge within the inner ring regions. It should be noted that
4 although negative charge density is measured experimentally, this cannot directly be attributed to the
5 presence of valence charge density. This is because the experimentally measured E-field is a vector
6 quantity, and any closed path of the vector field featuring a negative divergence will be reflected as a
7 negative charge density, even if the electric field arises from positive charges only. Further, we find
8 that it is important to account for the partial spatial and temporal coherence of the electron beam
9 during 4D-STEM image simulation, as both have a significant influence on the quantitative and
10 qualitative spatial profiles of the reconstructed electric fields and charge densities (Supp. Fig 6).
11 Once these effects are appropriately modelled, we find close agreement between first-principles
12 image simulation and the experimentally measured values. Although DFT is required for the
13 purposes of structural relaxation, first-principles electrostatic potentials are not required for image
14 simulation. Only minor differences between DFT-derived and IAM-derived image simulation were
15 found (Supp. Fig 7), and $|E_{PC}|$ results computed directly from DFT results (without image
16 simulation) showed a high degree of agreement with 4D-STEM simulation once sufficient smearing
17 was applied.

18 In a defect-free graphene lattice, long-range nanoscale fluctuations are negligible due to perfect
19 uniformity of atomic density. Defects, in contrast, create nanoscale perturbations of atomic density
20 yield longer-range charge fluctuations, depicted using a lowpass filter in figure 3c. The long-range
21 spatial variation of the charge density has negative value at the region of the heptagon, associated
22 with lower atomic density, and higher charge density at the site of the pentagon. One of the main
23 advantages of 4D-STEM compared to HRTEM is its lack of contrast inversion across spatial
24 frequencies. In figure 3d-f, we present an image-corrected phase contrast TEM image of a graphene
25 dislocation taken with a monochromated source. Because of their thinness and low atomic number

graphene monolayers are well-represented as weak-phase objects. Thus, at Scherzer defocus HRTEM images of graphene monolayers should be proportional to their projected electrostatic potential. Because electric field is the spatial gradient of electric potential, the 2D gradient of the TEM images should be proportional to $|\mathbf{E}_{PC}|$. As shown in Fig. 3f the local enhancement of $|\mathbf{E}_{PC}|$ measured in Fig. 2 using 4D-STEM is not present, presumably due to inefficient contrast transfer of low spatial frequencies near the Scherzer condition. The three-dimensional ‘hillock’ structure of the dislocation core further complicates the analysis, as changes to defocus on the order of ± 1 nm can cause the contrast associated with the region of $|\mathbf{E}_{PC}|$ enhancement (Fig. 2e) to invert and become darker than the surrounding pristine lattice (Supp. Fig. 8). The low signal-to-noise ratio of HRTEM necessitates multi-frame averaging to yield a smooth, differentiable image. This applies further limitations to the applicability of HRTEM to the study of nanoscale electrostatic fields.

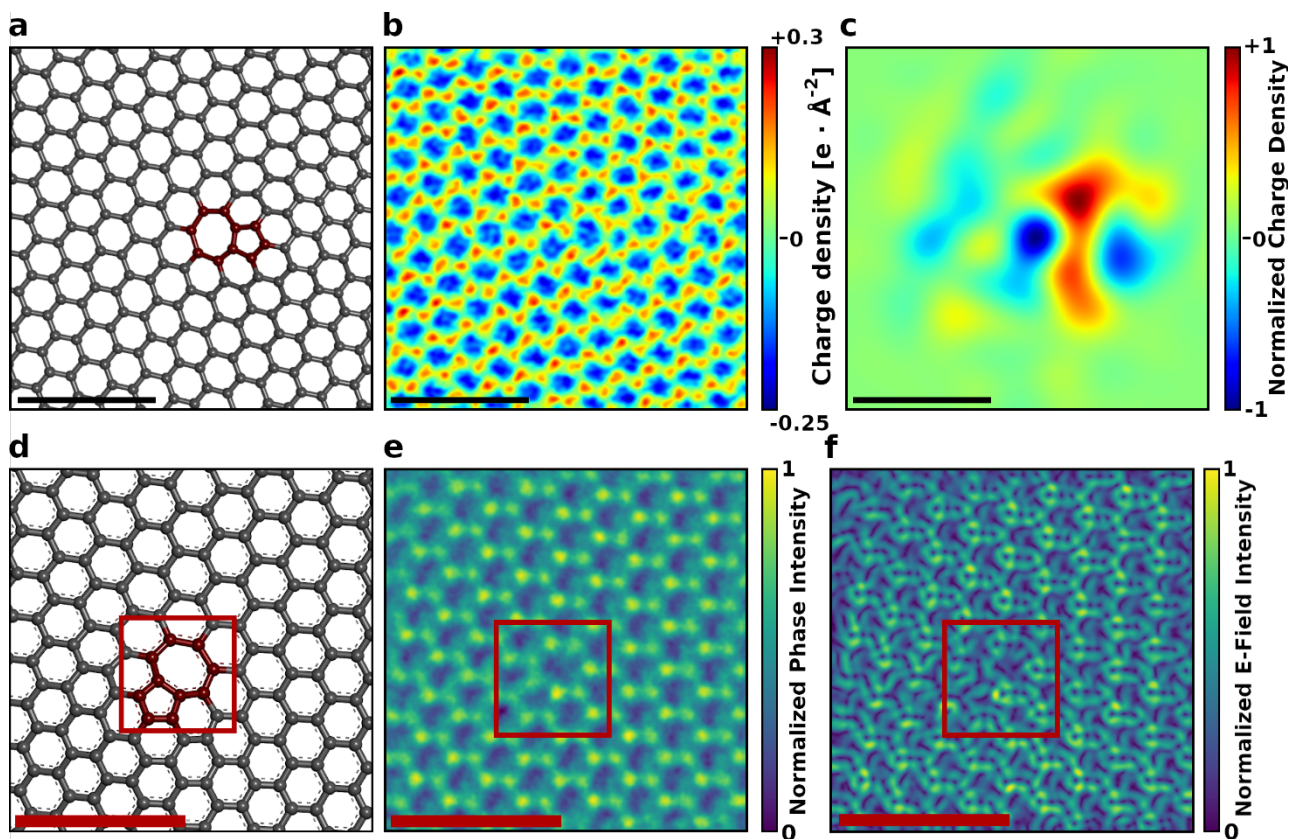


Figure 3: Experimental charge densities and comparison to HRTEM (a) Structural model of a graphene sheet with a (1,0) dislocation core highlighted in red. (b) Charge-density reconstruction of the (1,0) dislocation core, showing red (positive) density surrounding nuclear positions. Scale bar = 1 nm. (c) Low-pass-filtered image from (b), illustrating the surplus (red) and deficit (blue) of nuclear

charge density. Scale bar = 1 nm. (d) Structural model, showing a 5-7 dislocation core similar to those presented in the 4D-STEM study. (e) Aberration-corrected phase contrast TEM image of a graphene dislocation using a monochromated source. Image is an average of 5 images to increase signal-to-noise ratio. Although HRTEM images are proportional to phase, the exact phase-angle is difficult to estimate from the data, so the calibration bar has been left unitless. (f) Gradient of (e) shows features that are similar to $|\mathbf{E}_{PC}|$; however, units cannot be accurately determined, and the observed signal is modulated by a contrast transfer function, confounding quantitative study of $|\mathbf{E}_{PC}|$.

To understand how second-nearest-neighbor atoms contribute to the measured values of image simulations were carried out using an isolated heptagon (Fig. 4a, b, c) as compared to a heptagon-pentagon pair (Fig. 4d, e, f). Line profiles of taken around the inner core of the heptagon show only minor fluctuations. In contrast, the addition of three atoms to form a freestanding (1,0) dislocation core yields a significant change to the . This shows that the increased electric field magnitude can be explained by second nearest-neighbor distances and not from the asymmetry of the heptagon ring itself. A similar comparison showing $|\mathbf{E}_{PC}|$ distributions for a freestanding pentagon ring versus a freestanding heptagon ring can be seen in supporting figure 9 and the influence of out-of-plane bending is found to be minor, as shown in supporting figure 10. The pentagon contains the highest local density of atoms in the graphene sheet and gives rise to stronger momentum transfer to the electrons propagating within the inner region of the heptagon on the side neighboring the pentagon. These effects are not related to the electron charge distributions around the defect, but solely to the nanoscale variations in atomic density and subsequently the positive charge of the atomic nucleus.

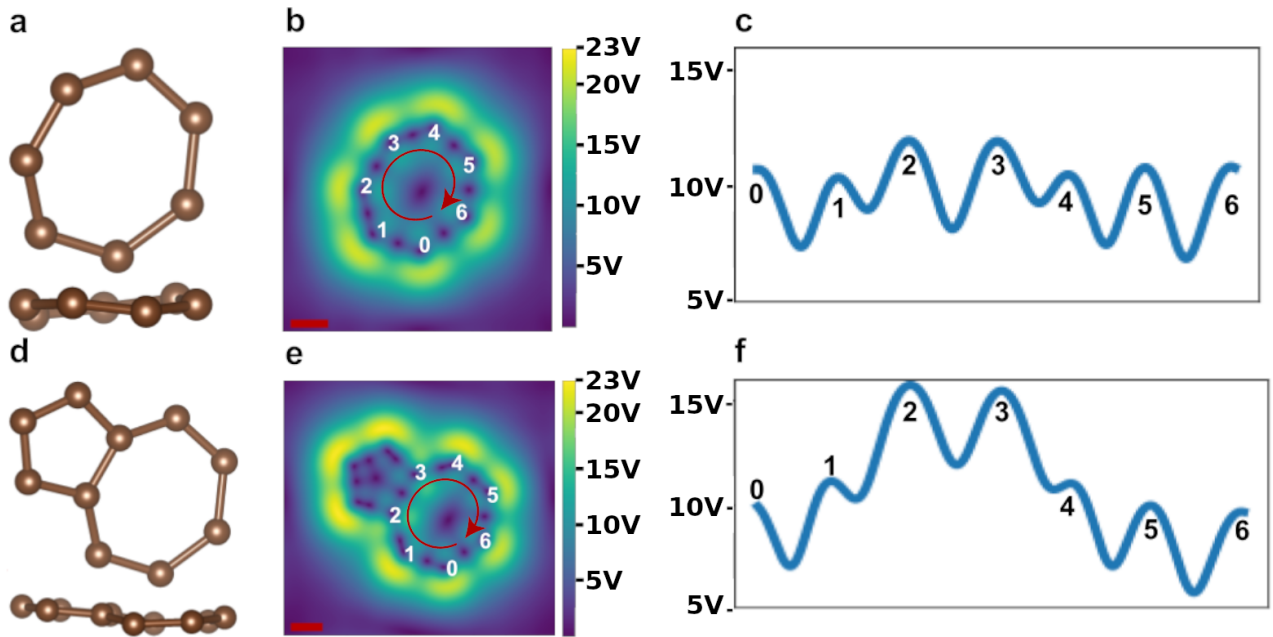


Figure 4: Effects of pentagon atoms on electric field enhancement. (a, d) Top-down and side-views of a model of a heptagon-ring (a) and a full heptagon-pentagon dislocation core (d). The effect of the 3D structural relaxation is apparent in side-view. (b, e) 4D-STEM $|E_{PC}|$ simulations calculated from the models in panel (a, d). Circumferential line profiles and vertex indices are indicated with red arrows and white text, respectively. Scale bars = 1 Å. (c, f) Line profiles from the paths indicated in (h, k), showing that the local $|E_{PC}|$ enhancement emerges primarily from the increase in nuclear charge density illustrated in (3a, 3c).

The effect of neighboring atoms on the qualitative spatial profile of $|E_{PC}|$ can be further understood through the study of low-angle grain boundaries (Fig. 5). Like dislocation lines, grain boundaries commonly produce pentagon and heptagon carbon rings in proximity; however, the resulting pentagon-heptagon cores may be oriented in the same direction (Fig. 5f), and it is also possible that multiple pentagon rings may adjoin one heptagon (Fig. 5e). In the latter case, the two adjoining pentagons, which are offset from one another by about 150° , largely cancel one another's influence, yielding a relatively flat profile of $|E_{PC}|$ (Fig. 5g, i, k). In contrast, the two aligned dislocation cores do not cancel out and behave similarly to the isolated dislocation cores studied earlier in the text. Supporting figure 11 shows that presence of two aligned pentagon-heptagon pairs should not be expected to measurably add together to increase the measured electrostatic field strength.

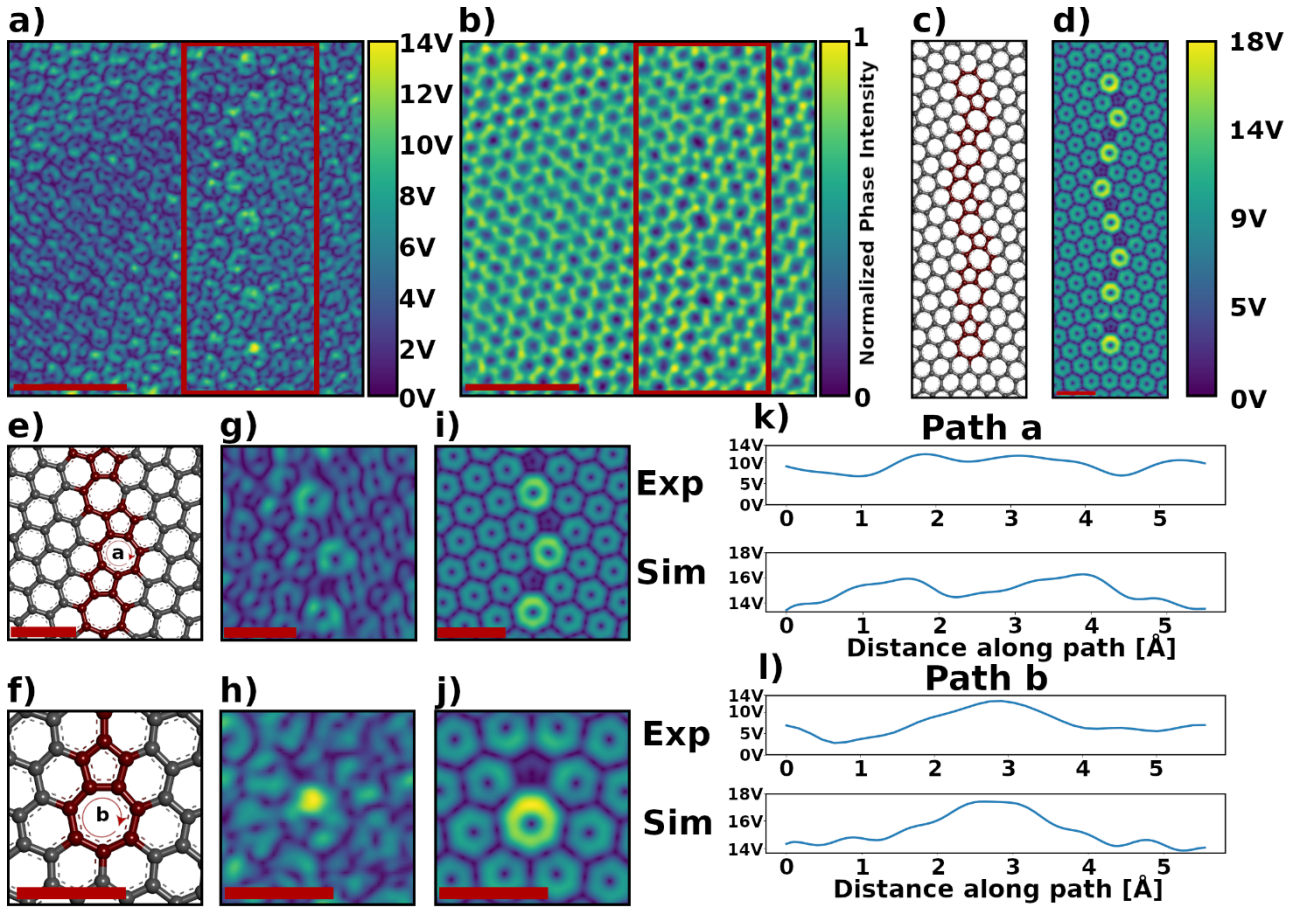


Figure 5: 4D-STEM study pentagon-heptagon pairs along grain boundaries (a, b) 4D-STEM $|E_{PC}|$ and phase images of a low-angle grain boundary. Inset white border corresponds to the field-of view of panels c & d. Scale bar = 10\AA . (c) Structural model of the low-angle grain boundary, with annotations depicting line plot paths a & b. Atomic positions for the structural model were determined from the phase image in panel b, as shown in supp. fig. 12. (d) Multislice simulation of $|E_{PC}|$, produced with the independent atom model using the model in (c). Scale bar = 5\AA . (e, f) Zoomed-in atomic models of ROIs, showing line plot paths a and b, respectively. (g, h) Zoomed-in views of $|E_{PC}|$ corresponding to the fields of view illustrated in (e, f). (i, j) 4D-STEM image simulation of the regions depicted in e through h. (k, l) Comparison of line plots from experimental and simulated $|E_{PC}|$ from paths a and b, respectively.

In this work, we analyze spatial fluctuations in electrostatic fields using 4D-STEM coupled with multislice STEM simulations and density functional theory. We show that center-of-mass 4D-STEM is more capable of measuring the local electrostatic environment than conventional phase-contrast TEM, due to its simpler contrast transfer function (Fig. 3) and direct measurement of momentum transfer, rather than object phase. Further, we find that 4D-STEM is sensitive to atomic structure in the neighborhood of the electron probe; a pronounced local enhancement of the projected, probe-convolved electrostatic field was observed within the part of the heptagon ring closest to the

1 adjoining pentagon. Through simulation, we find that the effect is unlikely to arise from the three-
2 dimensional relaxed structure of the graphene sheet. Instead, the effect arises primarily due to
3 slightly higher density of atomic nuclei in dislocation core's pentagon, meaning that the momentum
4 transfer to the probe from the sample is measurable at a distance of at least two bond lengths, despite
5 screening from the first row of neighboring atoms. These results show that asymmetry in structural
6 defects cause fluctuations in the local measurement of electric field, which may be useful for future
7 studies of how similar defects interact with adsorbed species on the surface of graphene through their
8 electric field. Defects are often key to a variety of interesting physical phenomena, and this study
9 may present an avenue towards future study of the role that structural defects play in surface
10 diffusion, molecular binding, and catalysis in similar 2D materials. Last, this study presents how
11 contrast features measured using 4D-STEM can be interpreted through systematic measurement and
12 simulation.

13 **Methods**

14 Graphene was grown using chemical vapor deposition (CVD) on a near-liquid Cu catalyst. After
15 inspection via scanning electron microscope and Raman spectroscopy, the graphene was spin-coated
16 with poly(methyl methacrylate) (PMMA, Fisher Scientific), etched using a 1M Ammonium
17 Persulfate solution, and transferred onto an in-situ heating chip (Dens Solutions, Delft, The
18 Netherlands). Samples were dried overnight, heated at $\sim 150^\circ\text{C}$ to promote adhesion, and immersed
19 in acetone to remove the sacrificial PMMA layer. ADF images and 4D-STEM data were recorded on
20 a JEOL ARM300CF located at the electron physical sciences imaging center (ePSIC) using a Merlin
21 Medipix3 direct pixelated electron detector at an accelerating voltage of 60 kV. Imaging was carried
22 out at an elevated temperature of $\sim 700^\circ\text{C}$ not only to ensure sample cleanliness but also to promote
23 increase thermal motion of vacancies, allowing the dislocation lines to grow sufficiently long that
24 interactions between the strain fields surrounding each dislocation core could be neglected. Low-
25 magnification images of the sample showing the clean surface of the monolayer graphene can be

seen in supporting figure 13. Although probe current measurements were not gathered during these specific experiments, using similar conditions on a similar microscope we estimate that the total electron dose associated with each 4D-STEM scan is approximately $3 \cdot 10^7 \text{ e}^- \cdot \text{\AA}^{-2}$, which would likely lead to significant sample damage at room-temperature conditions.

Supporting Information

Information about the methods used to compute the quantities reported, including electrostatic field intensity, charge density, and phase images. Details for the simulation of 4D-STEM data, as well as information about density functional theory calculations and processing of DFT outputs. Details on TEM simulation software and graphical software used for plotting and visualization. Background on the structural defect of interest, additional experimental and simulation-based measurements, the influence of partial spatial and temporal coherence, the effect of out-of-plane sample distortion, simulation-based analysis of an idealized low-angle grain boundary, construction of the grain boundary atomic model from experimental data, and overview of region of the sample from which the data was collected.

Acknowledgements

We thank Diamond Light Source for access and support in use of the electron Physical Science Imaging Centre (Instrument E02, proposal #EM20345). Support from National Center for Electron Microscopy in the Molecular Foundry (proposal #7031) was supported by the Office of Science, Office of Basic Energy Sciences, of the U.S. Department of Energy under Contract No. DE-AC02-05CH11231.

References

1. Bahart, F.; Kotakoski, J.; Krashenninnikov, A.V. Structural Defects in Graphene. *ACS Nano*. 2010, 5, 26-41.
 2. Wei, Y.; Wu, J.; Yin, H.; Shi, X.; Yang, R.; Dresselhaus, M. The nature of strength enhancement and weakening by pentagon-heptagon defects in graphene. *Nature Materials* 2012, 11, 759-763.
-
-
-

-
-
-
3. Liu, T.; Pao, P.; Chang, C. Effects of dislocation densities and distributions on graphene grain boundary failure strengths from atomistic simulations. *Carbon* 2012, 50, 3465-3472.
 4. Yazyev, O. and Louie, S. Topological defects in graphene: Dislocations and grain boundaries. *Physical Review B* 2018, 81, 195420.
 5. Ma, C.; Sun, H.; Du, H.; Wang, J.; Zhao, A.; Li, Q.; Wang, B.; Hou, J. Structural and electronic properties of an ordered grain boundary formed by separated (1,0) dislocations in graphene. *RCS Nanoscale* 2015, 7, 3055-3059.
 6. Červenka, J.; Flipse, C.F. Structural and electronic properties of grain boundaries in graphite: Planes of periodically distributed point defects. *Physical Review B* 2009, 79, 195429.
 7. López-Sancho, M.; de Juan, F.; Vozmediano, M. Magnetic moments in the presence of topological defects in graphene. *Physical Review B* 2009, 79, 075413.
 8. Červenka, J.; Katsnelson, M.I.; Flipse, C.F.J. Room-temperature ferromagnetism in graphite driven by two-dimensional networks of point defects. *Nature Physics* 2009, 5, 840-744.
 9. Jeong, B.; Ihm, J.; Lee, G. Stability of dislocation defect with two pentagon-heptagon pairs in graphene. *Physical Review B*. 2008, 78, 165403.
 10. Hashimoto, A.; Suenaga, K.; Gloter, A.; Urita, K.; Iijima, S. Direct evidence for atomic defects in graphene layers. *Nature*. 2004, 430, 870- 873.
 11. Robertson, A.; Allen, C.; Wu, Y.; He, K.; Olivier, J.; Neethling, J.; Kirkland, A.; Warner, J. Spatial control of defect creation in graphene at the nanoscale. *Nature Communications*. 2012, 3, 1144.
 12. Warner, J.; Margine, E.; Mukai, M.; Robertson, A.; Giustino, F.; Kirkland, A. Dislocation-Driven Deformations in Graphene. *Science*. 2012, 337, 209-212.
 13. Chuncheng, G.; Robertson, A.; He, K.; Lee, G.D.; Yoon, E.; Allen, C.; Kirkland, A.; Warner, J. Thermally Induced Dynamics of Dislocations in Graphene at Atomic Resolution. *ACS Nano* 2015, 9, 10066-10075.
 14. Lee, G.D.; Yoon, E.; He, K.; Robertson, A.; Warner, J. Detailed formation processes of stable dislocations in graphene. *Nanoscale* 2014, 6, 14836-14844.
 15. Lehtinen, O.; Kurasch, S.; Krasheninnikov, A.; Kaiser, U. Atomic scale study of the life cycle of a dislocation in graphene from birth to annihilation. *Nature Communications*. 2013, 4, 2098.
 16. Yang, H.; Pennycook, T.; Nellist, P. Efficient phase contrast imaging in STEM using a pixelated detector. Part II: Optimization of imaging conditions. *Ultramicroscopy* 2015, 151, 232-239.
 17. Lazić, I.; Bosch, E.; Lazar, S. Phase contrast STEM for thin samples: Integrated differential phase contrast. *Ultramicroscopy* 2016, 160, 265-280.
-
-
-

-
-
-
18. Yücelen, E.; Lazić, I.; Bosch, E. Phase contrast scanning transmission electron microscopy imaging of light and heavy atoms at the limit of contrast and resolution. *Scientific Reports* 2018, 8, 2678.
 19. Wen, Y.; Ophus, C.; Allen, C.; Fang, S.; Chen, J.; Kaxiras, E.; Kirkland, A.; Warner, J. Simultaneous Identification of Low and High Atomic Number Atoms Using 4D Scanning Transmission Electron Microscopy. *Nano Letters* 2019, 19, 6482-6491.
 20. Ophus, C. Four-Dimensional Scanning Transmission Electron Microscopy (4D-STEM): From Scanning Nanodiffraction to Ptychography and Beyond. *Microscopy and Microanalysis* 2019, 25, 563-582.
 21. Chen, Z.; Jiang, Y.; Shao, Y.; Holtz, M.; Odstrčil, M.; Guizar-Sicairos, M.; Hanke, I.; Ganschow, S.; Schlom, D.; Muller, D. Electron ptychography achieves atomic-resolution limits set by lattice vibrations. *Science* 2021, 372, 826-831.
 22. Jiang, Y.; Chen, Z.; Han, Y.; Deb, P.; Gao, H.; Xie, S.; Purohit, P.; Tate, M.; Park, J.; Gruner, S.; Elser, V.; Muller, D. Electron ptychography of 2D materials to deep sub-ångström resolution. *Nature* 2018, 559, 343-349.
 23. Müller-Caspary, K.; Duchamp, M.; Rösner, M.; Migunov, V.; Winkler, F.; Yang, H.; Huth, M.; Ritz, R.; Simson, M.; Ihle, S.; Soltau, H.; Wehling, T.; Dunin-Borkowski, R.; Van Aert, S.; Rosenauer, A. Atomic-scale quantification of charge densities in two-dimensional materials. *Physical Review B* 2018, 90, 121408.
 24. Müller-Caspary, K.; Krause, F.; Grieb, T.; Löffler, S.; Schowalter, M.; Béché, A.; Galioit, V.; Marquardt, D.; Zweck, J.; Schattschneider, P.; Verbeeck, J.; Rosenauer, A. Measurement of atomic electric fields and charge densities from average momentum transfers using scanning transmission electron microscopy. *Ultramicroscopy* 2017, 178, 62-80.
 25. Müller, K.; Krause, F.; Béché, A.; Schowalter, M.; Galioit, V.; Löffler, S.; Verbeeck, J.; Zweck, J.; Schattschneider, P.; Rosenauer, A. Atomic electric fields revealed by a quantum mechanical approach to electron picodiffraction. *Nature Communications* 2014, 5, 5653.
 26. Shibata, N.; Seki, T.; Sánchez-Santolino, G.; Findlay, S.; Kohno, Y.; Matsumoto, T.; Ishikawa, R.; Ikuhara, Y. Electric field imaging of single atoms. *Nature Communications* 2017, 8, 15631.
 27. Brown, H.G.; Shibata, N.; Sasaki, H.; Peterson, T.C.; Paganin, D.M.; Morgan, M.J.; Findlay, S.D. Measuring nanometre-scale electric fields in scanning transmission electron microscopy using segmented detectors. *Ultramicroscopy* 2017, 182, 169-178.
 28. Gao, W.; Addiego, C.; Wang, H.; Yan, X.; Hou, Y.; Ji, D.; Heikes, C.; Zhang, Y.; Li, L.; Huyan, H.; Blum, T.; Aoki, T.; Nie, Y.; Schlom, D.; Wu, R.; Pan, X. Real-space charge-density imaging with sub-ångström resolution by four-dimensional electron microscopy. *Nature* 2019, 575, 480-484.
 29. Fang, S.; Wen, Y.; Allen, C.; Ophus, C.; Han, G.; Kirkland, A.; Kaxiras, E.; Warner, J. Atomic
-
-
-

electrostatic maps of 1D channels in 2D semiconductors using 4D scanning transmission electron microscopy. *Nature Communications* 2019, 10, 1127.

30. Ishikawa, R.; Findlay, S.; Seki, T.; Sánchez-Santolino, G.; Kohno, Y.; Ikuhara, Y.; Shibata, N. Direct electric field imaging of graphene defects. *Nature Communications*. 2018, 9, 3878.

31. Wen, Y.; Fang, S.; Coupin, M.; Lu, Y.; Ophus, C.; Kaxiras, E.; Warner, J. Mapping 1D Confined Electromagnetic Edge States in 2D Monolayer Semiconducting MoS₂ using 4D-STEM. *ACS Nano*. 2022, 16, 6657-6665.

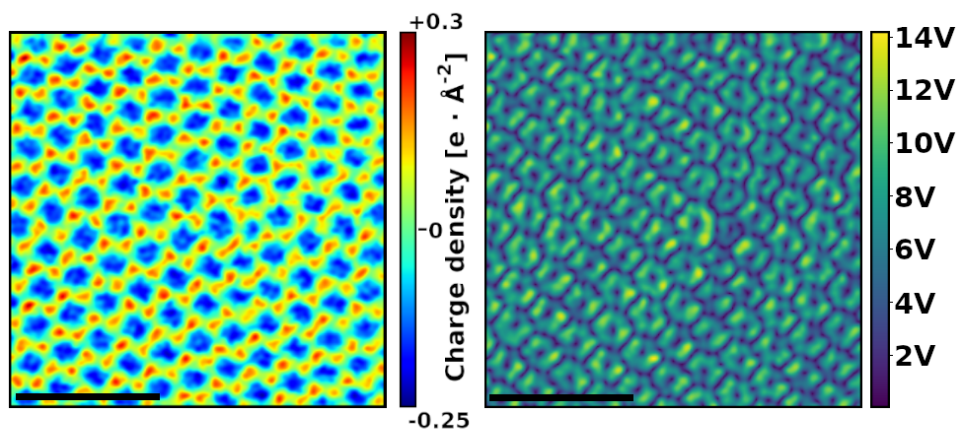
32. Cretu, O.; Ishizuka, A.; Yanagisawa, K.; Ishizuka, K.; Kimoto, K. Atomic-Scale Electrical Field Mapping of Hexagonal Boron Nitride Defects. *ACS Nano*. 2021, 15, 5316-5321.

33. Calderon, S.; Ferreira, R.; Taneja, D.; Jayanth, RT; Zhou, L.; Ribeiro, R.; Akinwande, D.; Ferreira, P. Atomic Electrostatic Maps of Point Defects in MoS₂. *Nano Letters*. 2021, 21, 10157-10164.

34. Robertson, A.; Montanari, B.; He, K.; Allen, C.; Wu, Y.; Harrision, N.; Kirkland, A.; Warner, J. Structural Reconstruction of the Graphene Monovacancy. *ACS Nano*. 2013, 7, 4495-4502.

1
2

TOC Graphic



3